Nano Research

Open Access

Research Article

An enzyme-gated bioorthogonal catalytic nanoreactor for tumor-specific prodrug activation

Yuheng Guo[1], Fang Jiang[1], Xiaohui Zhu[2], Wen He[1], Sijie Song[1], Xuecen Shou[1], Mengnan Wu[1], Ting Wu[1], Tingjing Huang[3], Zhi Ye[4], Xuyang Wang[1], Zhitong Chen[3], Yu He[1] ✉, Yuhang Yao[1] ✉, Zhaowei Chen[1] ✉, and Huanghao Yang[1]

[1] *New Cornerstone Science Laboratory, MOE Key Laboratory for Analytical Science of Food Safety and Biology, College of Chemistry, Fuzhou University, Fuzhou 350108, China*
[2] *Food Inspection and Quarantine Technical Center of Shenzhen Customs District of the People's Republic of China, Shenzhen 518045, China*
[3] *Institute of Biomedical and Health Engineering, Shenzhen Institute of Advanced Technology, Chinese Academy of Sciences, Shenzhen 518055, China*
[4] *Department of Chemistry, University College London, London WC1H 0AJ, UK*

Cite this article: *Nano Research*, **2025**, *18*, 94907134. https://doi.org/10.26599/NR.2025.94907134

ABSTRACT: Bioorthogonal catalysis mediated by abiotic transition metal catalysts (TMCs) is emerging as a momentum-gathering strategy for *in situ* generation of therapeutics. However, the unpredictable leakage and deposition of TMCs in living systems easily lead to nonspecific exposure of catalysts and concomitant off-target prodrug activation. Herein, we propose an enzyme-gated bioorthogonal catalytic nanoreactor constructed from hyaluronic acid (HA)-coated dendritic mesoporous silica nanoparticles (DMSNs), where the latter serves as a host for robustly immobilizing organometallic Ru(II) catalysts via covalent interactions. The covalent immobilization of catalysts within the nanoscaffold effectively avoids nonspecific metal leakage under biological conditions. Importantly, the grafted HA not only acts as a "gatekeeper" preventing unintended catalyst exposure in nontargeted tissues but also acts as a ligand targeting CD44 overexpressed cancer cells. Upon receptor-mediated endocytosis into tumor cells, HA is degraded by the overexpressed hyaluronidase-1, leading to the channel opening of the nanoreactors and hence gaining the accessibility of Ru(II) complexes to prodrugs. The therapeutic potency of this enzyme-gated nanoreactor in mediating site-specific activation of caged prodrugs was systematically demonstrated both in cellular settings and in tumor-bearing murine models. This enzyme-gated strategy enhances the efficacy of localized treatment while avoiding off-target prodrug activation, paving the way for advancing bioorthogonal catalysis for disease management in a safe and effective way.

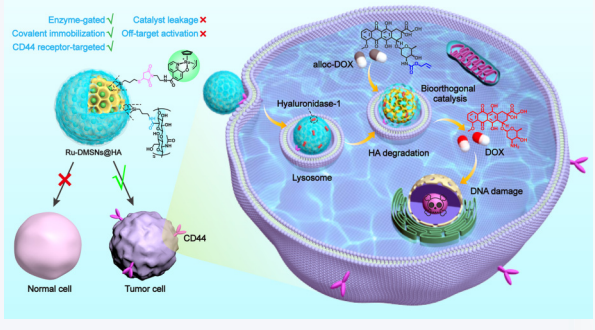

KEYWORDS: bioorthogonal catalysis, prodrugs, enzyme-gated, catalyst immobilization, cancer therapy

1 Introduction

Bioorthogonal chemistry provides unprecedented opportunities to interrogate and manipulate biological processes within complex living environments without interfering with native bioprocesses [1–7]. Within the realm of bioorthogonal chemistry, bioorthogonal catalysis mediated by abiotic transition metal catalysts (TMCs) holds tremendous biomedical potential [8–13]. As this class of nonnatural chemistry facilitates catalytic transformations inaccessible to natural enzymes, it allows for locoregional activation of high-dosed prodrugs exclusively where TMCs are located, widening the therapeutic window [14–17]. Considering the bioinertness of bioorthogonal prodrugs, the performance of TMCs is of paramount importance in the success of this therapeutic paradigm [18, 19]. To overcome the limitations of "naked" TMCs in terms of poor solubility, low biocompatibility, toxicity, and deactivation in biological milieu, bioorthogonal catalytic devices incorporating TMCs into micro-/nanoscaffolds have been developed as extracellular implants or intracellular reactors with improved catalytic efficiency [14–16, 20–28]. Nonetheless, in most cases, the immobilization of TMCs on scaffolds relies on relatively

Received: October 11, 2024; **Revised:** November 8, 2024
Accepted: November 11, 2024

✉Address correspondence to Yu He, heyu@fzu.edu.cn; Yuhang Yao, yuhangyao@fzu.edu.cn; Zhaowei Chen, chenzw@fzu.edu.cn

weak noncovalent interactions, like van der Waals forces, hydrogen bonding, and electrostatic interactions, making TMCs susceptible to detach from the support in the complex, reactive, and hostile bioenvironment [14, 29]. In addition, the complexity of high-level living systems poses substantial challenges in directing systemically administrated TMCs to accumulate at the site of interest [8, 9]. Regarding the supra-stoichiometric feature of bioorthogonal catalysis, the exposure of TMCs in healthy tissues due to metal leaching or off-target catalyst deposition, even at a low dose, can lead to unintended prodrug activation and accompanied side effects.

To address these challenges, we developed an enzyme-gated bioorthogonal nanoreactor for *in situ* prodrug activation within tumor cells (Scheme 1). This approach prevented TMC leakage by covalently anchoring organometallic Ru(II) complexes into the channels of dendritic mesoporous silica nanoparticles (Ru-DMSNs), the surface of which was further coated with hyaluronic acid (Ru-DMSNs@HA). The conjugated HA, a natural polysaccharide [30–32], can serve as a "gatekeeper" preventing the accessibility of the catalysts at nontargeted locations while conferring the nanoreactor targeting capability towards CD44 overexpressed cancer cells. Following receptor-mediated uptake by cancer cells into lysosomes, the cleavage of HA by the high-level intracellular hyaluronidase-1 (Hyal-1) gave rise to the opening of the channel of DMSNs, gaining accessibility of the inner anchored Ru(II) catalysts to their substrates. This rational design of the nanoreactor and its inherent bio-nano interfacial interactions effectively minimized unintended prodrug activation associated with uncontrolled metal leaching or nonspecific TMC deposition. The feasibility of this bioorthogonal catalysis strategy was fully demonstrated through cellular studies and by intratumor activation of systemically administered N-allyloxycarbonyl-caged doxorubicin in tumor-bearing murine models, which effectively suppressed the tumor growth while minimizing off-target drug exposure in the plasma and major organs.

2 Experimental

2.1 Preparation of dendritic mesoporous silica nanoparticles (DMSNs)

DMSNs with thiol group-modified inner surface and amino group-modified outer surface were prepared following a previously reported method [33]. Briefly, cetyltrimethylammonium tosylate (CTATos, 1.92 g) and triethanolamine (0.31 g) were dissolved in deionized water (100 mL) and stirred at 80 °C for 1 h. Then, tetraethyl orthosilicate (TEOS, 15.6 mL) was quickly added, and stirred at 80 °C for another 2 h. The synthesized DMSNs were collected by centrifugation, extensively washed with deionized water and ethanol, and dried in an oven at 80 °C overnight. Next, the unextracted DMSNs (1.0 g) was dispersed in toluene (100 mL) by sonication. (3-aminopropyl) triethoxysilane (APTES, 0.3 mL) was added, and the mixture was refluxed at 110 °C for 24 h. Since the mesopores were still blocked by surfactant during the

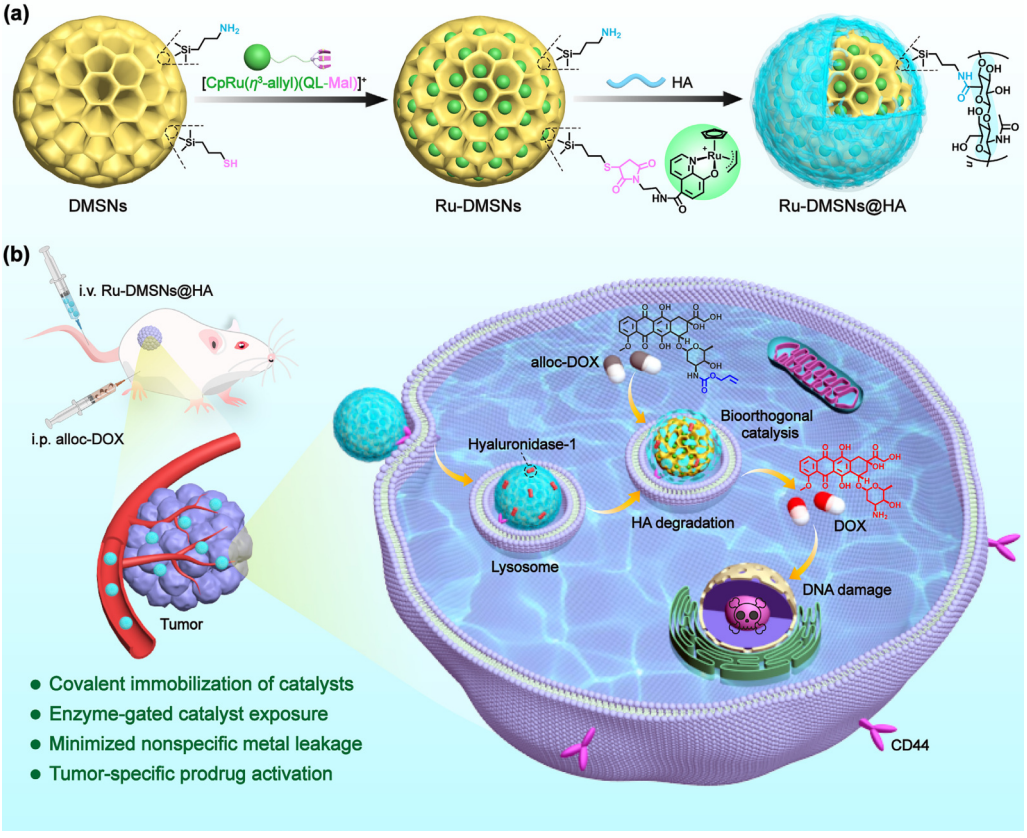

Scheme 1 Schematic illustration of an enzyme-gated bioorthogonal catalytic nanoreactor for site-specific activation of prodrugs within tumor cells. (a) Design and construction of the bioorthogonal catalytic nanoreactor through covalent immobilization of Ru(II) catalysts within the channels of HA-coated DMSNs. (b) Following receptor-mediated endocytosis into tumor cells, Ru-DMSNs@HA is internalized into lysosomes, where hyaluronidase-1 degrades HA, thereby opening the DMSN channels and enabling *in situ* prodrug activation. The combination of covalent immobilization and enzyme-responsive machinery effectively prevents metal leakage or nonspecific catalyst deposition associated off-target activation of systemically administered prodrugs.

grafting process, (3-aminopropyl) triethoxysilane preferentially condensed on the external surfaces of the DMSNs. The amino group-modified DMSNs were obtained by centrifugation, washed with ethanol, and dried in oven at 80 °C for overnight. To modify the inner surfaces of the DMSNs with thiol groups, the surfactant template CTATos in the pores of amino-group-modified DMSNs were extracted using a solution of 10% HCl in ethanol at 78 °C for 24 h, repeating this process three times. Subsequently, 3-mercaptopropyltrimethoxysilane (MPTMS, 0.3 mL) was added to toluene (100 mL) with uniformly dispersed amino-modified DMSNs (1.0 g). The mixture was refluxed for 12 h at 110 °C under an argon atmosphere. After completion, the product was collected by centrifugation, washed with ethanol three times, and dried under vacuum at 80 °C overnight to obtain the DMSNs with thiol-modified inner surface and amino group-modified outer surface.

2.2 Synthesis of rhodamine B-labeled DMSNs (DMSNs^{RITC})

Rhodamine B isothiocyanate (RITC, 4 mg) was reacted with 120 μL of APTES in 1 mL ethanol overnight in the dark. CTATos (1.92 g) and triethanolamine (0.31 g) were dissolved in deionized water (100 mL) and stirred at 80 °C for 1 h. Then, TEOS (15.48 mL) and APTES-modified dye solution was quickly added to the mixture and stirred at 80 °C for another 2 h. The resulting DMSNs^{RITC} was then modified with amino and thiol groups through a process similar to the preparation of DMSNs.

2.3 Preparation of Ru-DMSNs.

DMSNs (10 mg) were dispersed in phosphate-buffered saline (PBS, pH 7.0, 9.5 mL). A solution of compound 7 (1.5 mg) in dimethyl sulfoxide (DMSO, 0.5 mL) was added to the DMSNs suspension. The mixture was stirred at room temperature for 24 h. After completion, excess compound 7 was removed by centrifugation, and the crude product was washed with deionized water three times. The final product, Ru-DMSNs, was dried under vacuum overnight. Ru-DMSNs^{RITC} was synthesized using a similar procedure.

2.4 Preparation of Ru-DMSNs@HA

N-hydroxysuccinimide (NHS, 97.8 mg) and N-(3-dimethylaminopropyl)-N-ethyl carbodiimide hydrochloride (EDC, 52.8 mg) were added to a 2-(N-morpholino)ethane-sulfonic acid (MES) buffer (pH 6.0, 10 mL) solution containing hyaluronic acid (HA, M_W = 200 kDa, 30 mg). The mixture was stirred continuously at room temperature for 24 h. Then, Ru-DMSNs (30 mg) dispersed in deionized water (10 mL) was added to the solution of activated HA, and the pH was adjusted to 9.0 using triethylamine (TEA). The mixture was stirred at room temperature for another 24 h. After completion, the Ru-DMSNs@HA was collected by centrifugation, washed with deionized water three times, and dried under vacuum overnight. The Ru-DMSNs^{RITC}@HA was prepared using the same procedure for preparing Ru-DMSNs@HA.

2.5 Opening the gate of Ru-DMSNs@HA

Ru-DMSNs@HA (10 mg) was dispersed in acetate buffer (5 mL, pH 5.0), and hyaluronidase-1 (150 U/mL) was added to the suspension. The mixture was stirred at 37 °C for 2 h. After completion, the samples were centrifuged and washed with deionized water to obtain the Ru-DMSNs@HA*.

2.6 Deallylation activity of Ru-DMSNs

The deallylation activity of Ru-DMSNs was evaluated by the allylcarbamate cleavage of alloc-RhB 110. Specifically, a stock solution of alloc-RhB 110 (100 μL, 100 μM) in DMSO was added to a centrifugal tube. 900 μL of Ru-DMSNs or fRu solution in PBS buffer (pH 7.4) was added to this solution, resulting in a final concentration of 10 μM of alloc-RhB 110 and Ru-DMSNs (with Ru content of 5 μM) or 5 μM of fRu. The mixture was then shaken at 500 rpm and 37 °C in a thermomixer. At various time points, the nanoreactors were isolated by centrifugation, and 5 μL of the supernatant was diluted with 95 μL of deionized water. The fluorescence intensity was measured using a microplate reader. The conversion kinetics was determined based on fluorescence intensity measurements (excitation/emission = 488/521 nm) and calculated using a standard curve of RhB 110. A control experiment with alloc-RhB 110 alone was conducted following the same protocol. Similar procedures and analyses were applied for reaction occurring in buffer solutions with varying pH values (4.5 to 7.4).

2.7 Enzyme-gated catalytic performance of Ru-DMSNs@HA

A stock solution of alloc-RhB 110 (100 μL, 100 μM) in DMSO was added to a centrifugal tube, followed by the addition of 900 μL of Ru-DMSNs@HA or Ru-DMSNs@HA* in PBS buffer (pH 7.4), resulting in a final concentration of 10 μM of alloc-RhB 110 with the final Ru content of 5 μM. The mixture was then shaken at 500 rpm and 37 °C in a thermomixer. At various time points, the nanoreactors were isolated by centrifugation, and 5 μL of the reaction medium was withdrawn, diluted with 95 μL of deionized water, and analyzed for fluorescence intensity using a microplate reader. Conversion (%) was determined from fluorescence intensity measurements (excitation/emission = 488/521 nm) and calculated using a standard curve of RhB 110. Similar procedures and analyses were applied for reactions carried out in Dulbecco's modified Eagle's medium (DMEM), DMEM plus 10% fetal bovine serum (FBS), and lysates of 4T1 and NIH3T3 cells. Additionally, the same method was applied to reaction conducted with fRu under different conditions.

2.8 Reusability of Ru-DMSNs@HA*

After completing the above reaction, Ru-DMSNs@HA* was recovered by centrifugation at 13,000 rpm for 30 min. A fresh solution of alloc-RhB 110 (10 μM) in PBS was added to the recovered Ru-DMSNs@HA*. The mixture was shaken at 500 rpm and 37 °C in a thermomixer, and the reaction progress were monitored after 12 h using a microplate reader (excitation/emission = 488/521 nm). This cycle was repeated five times.

2.9 Assessment of catalyst leakage from the nanoreactor

In a typical experiment, Ru-DMSNs@HA or Ru-DMSNs@HA* (with the final Ru content of 5 μM) was dispersed in 900 μL PBS buffers, cell culture medium, or cell lysate and incubated for 24 h. After that, the solid part was removed by centrifugation, and the supernatant was collected. The supernatant was then concentrated, digested with aqua regia, and analyzed using inductively coupled plasma mass spectrometry (ICP-MS). Additionally, the alloc-RhB 110 (100 μL, 100 μM) was added to the supernatant. The resulting solution was shaken at 500 rpm and 37 °C in a thermomixer, and the fluorescence intensity was measured using a microplate reader.

2.10 Prodrug activation by the nanoreactor

Alloc-DOX (100 μL, 1 mM) was dissolved in PBS (0.9 mL) containing Ru-DMSNs@HA or Ru-DMSNs@HA* (with the final Ru content of 50 μM). The mixture was shaken at 500 rpm and 37 °C in a thermomixer. At specified time points, the nanoreactors were removed by centrifugation, and 10 μL of the reaction medium was mixed with 90 μL of methanol. After centrifugation at 12,000 rpm for 10 min, the supernatant was analyzed by high-performance liquid chromatography (HPLC). The HPLC analysis was performed using a Waters Alliance e2695 system equipped with a Kromasil C18 HPLC column (particle size, 5 μm; pore size, 300 Å; length by inner diameter, 250 mm × 4.6 mm) at a constant flow rate of 1.0 mL/min and a column temperature of 25 °C. The mobile phase comprised deionized water and acetonitrile with 0.1% trifluoroacetic acid (68:32) over 18 min. Chromatograms were documented by measuring the ultraviolet absorbance at λ = 254 nm.

2.11 Cell culture

All cell lines were supplied by American Type Culture Collection (ATCC, Manassas, VA). 4T1 cells and NIH3T3 cells were cultured in DMEM supplemented with 10% FBS and 1% penicillin/streptomycin. All cells were maintained in an incubator at 37 °C with 5.0% CO_2.

2.12 Preparation of cell lysate

4T1 or NIH3T3 cells, cultured to 80%–90% confluency in a T75 flask, were collected by trypsinization and then centrifuged. The cells were washed twice with PBS, followed by treatment with 5 mL of PBS (pH 6.0) containing 1% RIPA lysis buffer for 30 min at 4 °C. The crude lysate was then centrifuged at 3000 rpm for 15 min, and the supernatant was collected to obtain the cell lysate.

2.13 Cytotoxicity assay

The cytotoxicity of Ru-DMSNs@HA to 4T1 and NIH3T3 cell lines were assessed using the CCK-8 assay. Cells were seeded in 96-well plates at a density of 1×10^4 cells per well. After 24 h of incubation, the medium was removed, and the cells were washed twice with PBS. The cells were then treated in triplicate with 100 μL of Ru-DMSNs@HA at varying concentrations (0, 5, 10, 25, 50, 100, 150, and 200 μg/mL) and further cultured for 48 h. Subsequently, the culture medium was replaced with a 10% CCK-8 reagent solution, and the cells were incubated for 1 h at 37 °C. Absorbance was measured using a microplate reader at 450 nm, and the cell viability was calculated based on the absorbance readings.

2.14 Cellular uptake and subcellular localization

4T1 and NIH3T3 cells were seeded in confocal dishes (35 mm) at a density of 1×10^5 cells per well. After 24 h, Ru-DMSNs^{RITC}@HA (50 μg/mL) was added and incubated with the cells for 0.5, 1, 2 and 4 h. The cells were then washed three times with DMEM plus 10% fetal bovine serum (DMEM-FBS), stained with Lysotracker Green for 30 min, and subsequently with Hoechst 33342 for 15 min. Finally, fluorescence imaging was performed using a Nikon SIM confocal laser scanning microscope. For flow cytometric analysis, cells were treated similarly to the confocal microscopy samples, except that Hoechst 33342 staining was omitted. Instead, the cells were harvested and resuspended in PBS. To confirm HA receptor-mediated endocytosis of Ru-DMSNs^{RITC}@HA, 4T1 cells were preincubated with an excess amount of HA (5 mg/mL) for 2 h before the addition of Ru-DMSNs^{RITC}@HA. The other steps were conducted as described above.

2.15 Ru-DMSNs^{RITC}@HA mediated bioorthogonal catalysis in living cells

4T1 and NIH3T3 cells were seeded in the confocal dishes (35 mm) at a density of 1×10^5 cells per well. After 24 h, the culture medium was replaced with fresh culture medium containing Ru-DMSNs^{RITC}@HA (50 μg/mL), and the cells were incubated with Ru-DMSNs^{RITC}@HA for 4 h. Following incubation, the cells were washed with DMEM-FBS to remove extracellular nanoreactors. Fresh media containing 10 μM alloc-RhB 110 was then added, and the cells were incubated for various time points. Subsequently, the cell nuclei were stained with Hoechst 33342 for 15 min, and fluorescence images were captured using a Nikon SIM confocal laser scanning microscope. For flow cytometric analysis, cells were treated similarly, except that Hoechst 33342 staining was omitted. The cells were harvested and resuspended in PBS. To further demonstrate the enzyme-gated behavior of Ru-DMSNs^{RITC}@HA within cells, 4T1 cells were preincubated with neomycin sulfate (50 μg/mL, a Hyal-1 inhibitor) for 6 h before the addition of Ru-DMSNs^{RITC}@HA. The other steps were conducted as described above.

2.16 Cellular viability assays

The cytotoxicity of Doxorubicin (DOX) and alloc-DOX were evaluated using the CCK-8 assay. 4T1 cells were seeded in 96-well plates at a density of 1×10^4 cells per well. After 24 h, the cells were treated with DOX or alloc-DOX at a range of concentrations from 1 nM to 100 μM and cultured for 48 h. For the alloc-DOX/Ru-DMSNs@HA combination group, cells were first treated with 50 μg/mL Ru-DMSNs@HA for 4 h, followed by washing to remove the extracellular nanoreactors. Fresh media containing various concentrations of alloc-DOX were then added, and the cells were incubated for another 48 h. Subsequently, the culture medium was replaced with a 10% CCK-8 reagent solution, and the cells were incubated for 1 h at 37 °C. Finally, absorbance was measured at 450 nm using a microplate reader, and the cell viability was calculated based on the absorbance readings. For control experiments, the 4T1 cells were preincubated with either an excess amount of HA (5 mg/mL) for 2 h or neomycin sulfate (50 μg/mL) for 6 h before the addition of Ru-DMSNs^{RITC}@HA. The other steps were carried out as described above.

2.17 Determination of 4T1 cell apoptosis

4T1 cells were seeded in 6-well plates at a density of 2×10^5 cells per well. After 24 h, the cells were treated with DMSO (1%), Ru-DMSNs@HA (50 μg/mL), DOX (5 μM), alloc-DOX (5 μM), and Ru-DMSNs@HA (50 μg/mL) plus alloc-DOX (5 μM) for another 24 h. Apoptosis in 4T1 cells following various treatments was assessed using terminal deoxynucleotidyl transferase dUTP nick-end labeling (TUNEL) staining, following the instructions provided in the One Step TUNEL Apoptosis Assay Kit. Additionally, dual-staining apoptosis assays were performed using flow cytometry according to the manufacturer's protocol.

2.18 Measurement of intracellular DOX levels

The prodrug activation capability of Ru-DMSNs@HA in a cell culture was examined by quantifying intracellular DOX using HPLC. 2×10^5 4T1 cells or NIH3T3 were seeded in 12-well plates

and subjected to various treatments. For monotherapy, the cells were incubated with 5 μM DOX or alloc-DOX for 24 h. For the combination treatments, cells were preincubated with 50 μg/mL Ru-DMSNs@HA for 4 h and washed with DMEM-FBS twice. The cells were then transferred to fresh DMEM containing 5 μM alloc-DOX and incubated for an additional 24 h. For control experiments, the 4T1 cells were preincubated with an excess amount of HA (5 mg/mL) for 2 h or neomycin sulfate (50 μg/mL) for 6 h before the addition of Ru-DMSNs@HA. The other steps were conducted as described above. All treated cells were washed three times with PBS and lysed by sonication. The supernatants were collected by centrifugation at 12,000 rpm for 15 min and concentrated under vacuum. The resulting solution was mixed with 0.5 mL of acetonitrile to denature proteins and extract dissolved compounds. The supernatant was then analyzed by HPLC to determine intracellular DOX levels.

2.19 Animal experiments

All animal procedures were approved by the Institutional Animal Care and Use Committee of Fuzhou University (protocol number: 013-20200610-002). Healthy female BALB/c mice (6–8 weeks old, ~ 20 g body weight) were purchased from Shanghai SLAC laboratory Animal Co., Ltd. All animal handling procedures adhered to the guidelines of the Regional Ethics Committee for Animal Experiments.

2.20 Pharmacokinetics of Ru-DMSNs@HA and fRu

To assess *in vivo* pharmacokinetics, female BALB/c mice were intravenously injected with Ru-DMSNs@HA at a dose of 20 mg/kg or fRu at a dose of 1.4 mg/kg. Blood samples (20 μL) were collected from the tail veins at 0.25, 0.5, 1, 2, 4, 6, 8, 12, and 24 h post-injection and dispersed in 480 μL aqua regia to dissolve the remaining Ru-DMSNs@HA or fRu. The concentration of Ru ions was then quantified using ICP-MS.

2.21 Biodistribution of Ru-DMSNs@HA and fRu

For biodistribution analysis, 4T1 tumor-bearing mice were intravenously injected with Ru-DMSNs@HA (20 mg/kg) or fRu (1.4 mg/kg). At specified time points post-injection, the mice were sacrificed, and their organs and tumors were harvested, weighed, and digested using aqua regia at 80 °C for three days. The Ru content in these samples was quantified using ICP-MS.

2.22 *In vivo* anti-tumor therapy

Tumor-bearing mouse models were established by subcutaneously injecting 1.0×10^6 luciferase-tagged 4T1 cells suspended in PBS into the right flank of each mouse. Once the tumor volume reached approximately 50–150 mm^3, the mice were randomly divided into 5 groups (n = 5, each group) and administered the following treatments every three days for a total of four doses, on day 0, 3, 6 and 9: (1) alloc-DOX (100 mg/kg)/Ru-DMSNs@HA (20 mg/kg) combination; (2) DOX (5 mg/kg); (3) alloc-DOX (100 mg/kg); (4) Ru-DMSNs@HA (20 mg/kg); (5) saline. For group (1), alloc-DOX was administered intraperitoneally 6 h after intravenous injection of Ru-DMSNs@HA. Tumor growth was monitored using bioluminescence imaging after intraperitoneal injection of luciferin (150 mg/kg) with images captured using IVIS Lumina III Series system (PerkinElmer). Tumor volume and body weight were recorded every 3 days. Tumor volume was measured using a vernier caliper and calculated using the formula: length × $width^2$ × 0.5. Mice showing signs of impaired health or with tumor volume exceeded 1500 mm^3 were euthanized with CO_2. At the end of the treatment, mice were sacrificed, and blood samples were collected for a complete blood panel and serum biochemistry analysis. Major organs (heart, liver, spleen, lung and kidney) were then collected and processed for hematoxylin and eosin (H&E) staining and TUNEL analysis to evaluate potential toxicities and cell death mechanism. Additionally, serum inflammatory cytokines (IFN-γ, TNF-α, IL-12 and IL-6) were measured 24 h post-injection using enzyme-linked immunosorbent assay (ELISA) kits from Invitrogen, Thermo Fisher Scientific, according to the manufacturer's instructions.

2.23 Statistical analysis

Data were collected from at least three separate measurements. Data are presented as the mean ± standard deviation (s.d.). Statistical analysis was performed using Student's t-test (two group) and one-way analysis of variance (ANOVA) with Tukey post-hoc tests (multiple comparison). $^*P < 0.05$, $^{**}P < 0.01$, $^{***}P < 0.001$, and $^{****}P < 0.0001$ indicate levels of statistical significance, while ns denotes no significance.

3 Results and discussion

3.1 Preparation and characterization of Ru-DMSNs@HA

To construct the proposed bioorthogonal catalytic nanoreactor, we initially prepared DMSNs with thiol group-modified inner surface and amino group-modified outer surface [33]. The obtained DMSNs exhibited a uniform spherical morphology with an average diameter of 120.2 nm and an average pore size of 15.83 nm (Fig. 1(a); Fig. S1 and Table S1 in the Electronic Supplementary Material (ESM)). Additionally, the DMSNs possessed a Brunauer–Emmett–Teller (BET) surface area of 333.64 m^2/g and a pore volume of approximately 1.47 cm^3/g, which would provide ample space for catalyst immobilization. The presence of these functional groups was confirmed by characteristic peaks in the Fourier transform infrared spectroscopy (FT-IR) spectra, including the sulfydryl stretching vibration at 2560 cm^{-1} and the peak assigned to amino groups at 1548 cm^{-1} (Fig. 1(b)). Next, we synthesized maleimide-terminated Ru(II) complex, [CpRu(η^3-allyl)(QL-Mal)]PF_6 (Cp = η^5-cyclopentadienyl, QL-Mal = 8-hydroxyquinoline derivative with a terminal maleimide group; Schemes S1 and S2, and Figs. S2–S4 in the ESM), as the TMC and then attached it onto the DMSNs inner surface via the thiol-Michael click addition reaction, resulting in Ru-DMSNs (Fig. 1(c)). The immobilization of Ru(II) complexes was confirmed by the color change of the samples from white to brown (insets in Figs. 1(a) and 1(c)), the appearance of a C=O stretching vibrations band at 1709 cm^{-1} the intensity of the peak at 2560 cm^{-1} in the FT-IR spectrum (Fig. 1(b)), and the presence of Ru (Ru3p) peaks (Fig. 1(d)) and the variation of the C1s signal (Figs. S5 and S6 in the ESM) in the X-ray photoelectron spectroscopy (XPS) spectra.

Thereafter, the obtained Ru-DMSNs were coated with HA through the formation of amide bonds between the carboxyl groups of HA and the amino groups on the outer surface of DMSNs to prepare the nanoreactor (Ru-DMSNs@HA). Compared to Ru-DMSNs, the obtained Ru-DMSNs@HA displayed a distinct border and a slight increase in the average diameter (124.5 nm) under TEM imaging, confirming the conjugation of HA (Fig. 1(e)). This

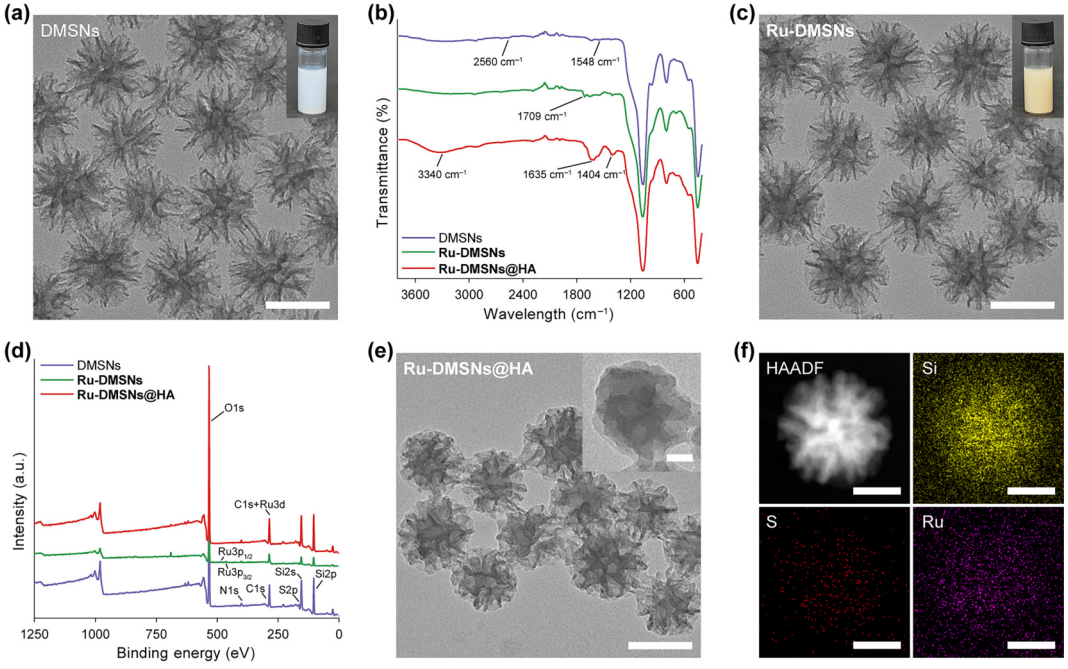

Figure 1 Preparation and characterization of Ru-DMSNs@HA nanoreactors. (a) TEM image of DMSNs. Scale bar: 100 nm. Inset: photograph of the suspension of DMSNs. (b) FT-IR spectra of DMSNs, Ru-DMSNs and Ru-DMSNs@HA. (c) TEM image of Ru-DMSNs. Scale bar: 100 nm. Inset: photograph of the suspension of Ru-DMSNs. (d) XPS spectra of DMSNs, Ru-DMSNs and Ru-DMSNs@HA. (e) TEM images of Ru-DMSNs@HA. Scale bar: 100 nm. Inset: high-resolution TEM image of Ru-DMSNs@HA. Scale bar: 25 nm. (f) Elemental mapping analysis of Ru-DMSNs@HA. HAADF, high-angle annular dark-field. Scale bars: 50 nm.

was further validated by the broad bands corresponding to amide C=O stretching in the ranges of 1200–1700 cm^{-1} (Fig. 1(b)), the negatively charged surface potential of –32.6 mV (Fig. S7 in the ESM), and XPS analysis (Fig. S8 in the ESM). Elemental mapping analysis revealed the uniform distribution of Ru elements within the nanoreactor (Fig. 1(f)), and the content of Ru was quantified to be 1.68 wt% using inductively coupled plasma mass spectrometry (ICP-MS; Table S2 in the ESM).

We next studied the colloidal stability of the nanoreactor in various aqueous solutions, including PBS (pH 7.4), saline (0.9% NaCl), cell culture medium (DMEM), and DMEM-FBS (Fig. S9 in the ESM). The Ru-DMSNs@HA remained well-dispersed without any signs of precipitation or aggregation, and there were no significant changes in their hydrodynamic sizes over 48-h standing in these solutions (Fig. S10 in the ESM). The remarkable colloidal stability of Ru-DMSNs@HA can be attributed to the strongly negatively charged surface provided by HA, in line with the conventional understanding that a zeta potential below –30 mV indicates a colloidal stable system [34]. This stability is advantageous for the circulation of the nanoreactor in the bloodstream and its accumulation in tumors through the enhanced permeation and retention (EPR) effect [35, 36].

3.2 Enzyme-gated catalysis in solution

Next, we evaluated the catalytic reactivity of Ru-DMSNs@HA using bis-*N*,*N*'-allyloxycarbonyl rhodamine 110 (alloc-RhB 110; Scheme S3 and Figs. S11–S13 in the ESM) as a model substrate. The reactions were conducted with 5 μM Ru and 2 equivalents of alloc-RhB 110 and monitored by recording the fluorescence of the regenerated rhodamine 110 (RhB 110; Fig. 2(a)). Initially, we compared the catalytic performance of Ru-DMSNs and free Ru(II) complexes (fRu; Scheme S4 and Figs. S14–S16 in the ESM) without terminal maleimide in PBS buffer. Both catalysts exhibited high activity in decaging alloc-RhB 110, with no significant differences in conversion efficiencies, initial reaction rates, or turnover numbers (Fig. 2(b) and Table S3 in the ESM), implying that covalent immobilization of Ru(II) complexes into the channels of DMSNs well preserved their reactivity. In addition, the activities of both Ru-DMSNs and fRu did not change much across buffer solutions with varying pH values (4.5 to 7.4) (Fig. S17 in the ESM). The comparable activity of Ru-DMSNs to fRu can be attributed to the presence of Ru(II) complexes as site-isolated reaction centers on the nanoscaffold [37], the high local concentration of catalysts within confined environments without aggregation, and the inherent mesoporous structure and large specific surface area of DMSNs, which together facilitated the substrates to diffuse within in the scaffold and contact with the catalysts.

Next, we investigated the enzyme-gated catalytic performance of Ru-DMSNs@HA in PBS, with or without pretreatment with Hyal-1 for 2 h under acidic conditions resembling those of lysosomes, in which HA is degraded after receptor-mediated uptake by cancer cells [38, 39]. For Hyal-1 pretreated Ru-DMSNs@HA (denoted as Ru-DMSNs@HA*; Fig. S18 in the ESM), fluorescence increased after mixing with alloc-RhB 110 and the conversion reached 80% after 8 h. In contrast, intact Ru-DMSNs@HA gave a rather low yield of RhB 110 (< 3%) over the same period (Fig. 2(c)). To further replicate this enzyme-gated catalysis in biologically more relevant media, we conducted similar experiments in DMEM, DMEM plus 10% FBS, and lysates of 4T1 and NIH3T3 cells. For untreated Ru-DMSN@HA, there was no significant improvement in the conversion of alloc-RhB 110 in DMEM and DMEM plus 10% FBS compared to PBS (Fig. 2(d)). However, the generation of RhB 110 in 4T1 cell lysates was 3.5-fold higher than that in NIH3T3 cell lysates, attributive to the higher expression level of Hyal-1 in cancer cells. These findings signify the gatekeeper function of HA against nonspecific opening in different scenarios, effectively controlling

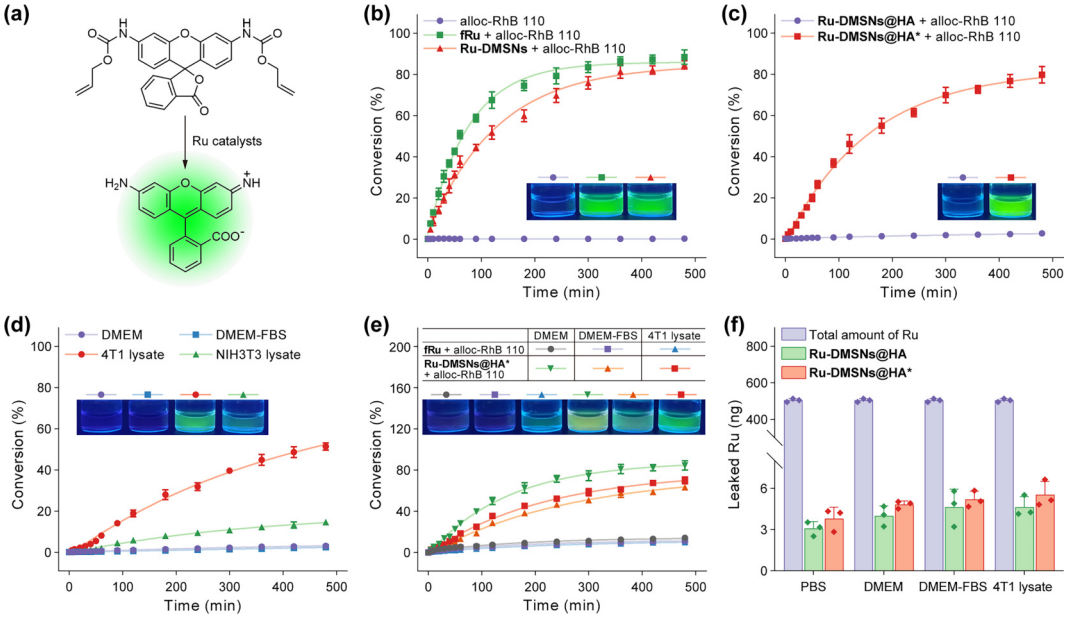

Figure 2 Catalytic activity of nanoreactors in solution. (a) Schematic representation of decaging non-fluorescent alloc-RhB 110 into fluorescent RhB-110. Kinetic profiles of alloc-RhB 110 decaging reactions catalyzed by (b) Ru-DMSNs and fRu in PBS solution (pH = 7.4), (c) Ru-DMSNs@HA* and Ru-DMSNs@HA in PBS solution (pH = 7.4), (d) Ru-DMSNs@HA in DMEM, DMEM-FBS, 4T1 and NIH3T3 lysates, and (e) Ru-DMSNs@HA* and fRu in DMEM, DMEM-FBS and 4T1 lysate. Inset: photograph of the reaction mixtures under ultraviolet light. (f) Analysis of Ru leakage from Ru-DMSNs@HA and Ru-DMSNs@HA* in PBS, 4T1 lysate, DMEM and DMEM plus 10% FBS solution over 24 h. Data points represent mean ± s.d. (n = 3 independent experiments).

the accessibility of the inner anchored Ru(II) catalysts. In parallel, for Ru-DMSNs@HA*, although a certain decrease in catalytic activity was observed in cell culture medium and cell lysates, the reactivity remained high and, specifically, the decline in conversion efficiency was 4.8-fold lower than that observed for fRu (Fig. 2(e)). This underscores the protective effect of the mesoporous nanoscaffold, which reduces the chances of catalyst deactivation caused by nonspecific protein binding or catalyst poisoning by biomolecules [29], thereby preserving of the catalytic performance of the nanoreactor after gate opening inside cancer cells.

To emphasize the advantages of covalent immobilization of Ru(II) complexes into DMSNs, we next investigated the possibility of catalyst leaching from the nanoreactor. For intact Ru-DMSNs@HA, minimal Ru leakage was detected by ICP-MS analysis after 24-h dispersion in PBS, cell culture medium, or cell lysates (Fig. 2(f)). After removing Ru-DMSNs@HA by centrifugation and introducing alloc-RhB 110 into the supernatant, there was no generation of fluorescence observed (Fig. S19 in the ESM), further confirming the stability of Ru-DMSN@HA against catalyst leaching. Similarly, for Hyal-1 pretreated Ru-DMSNs@HA, almost no Ru leakage was observed in these situations (Fig. 2(f)) and negligible decaging of alloc-RhB 110 occurred in the resulting supernatants (Fig. S20 in the ESM). After five runs of recycled catalysis, Ru-DMSNs@HA* displayed only a marginal reduction in catalytic conversion efficiency (Fig. S21 in the ESM). Additionally, the catalytic activity of Ru-DMSNs@HA remained low after one week of storage in PBS, but it was fully restored following treatment with Hyal-1 and the activity showed no difference compared to that of freshly prepared ones (Fig. S22(a) in the ESM), indicating that Ru-DMSNs@HA can maintain its catalytic activity and enzyme-gated property over the long term. The absence of significant changes in zeta potential and hydrodynamic diameter (Figs. S22(b) and S22(c) in the ESM) further demonstrates the long-term stability of Ru-DMSNs@HA. Moreover, only trace amount of Ru leakage was detected in PBS after one week of storage, confirming the coordination stability of the Ru(II) complex with its ligands (Fig. S22(d) in the ESM). This long-term stability, enzyme-gated property and the robustness against TMC leakage would help to prevent unexpected bioorthogonal catalytic reactions at non-targeted sites while the minimal reactivity loss in recycled catalysis allows for prolonged action following cellular uptake.

3.3 Intracellular activated bioorthogonal catalysis

Having demonstrated the enzyme-gated feature of Ru-DMSNs@HA in solution, we moved on to repeat this propensity under cellular conditions. Initially, we examined the cellular uptake efficiency of Ru-DMSNs@HA by 4T1 cells (which overexpress CD44, a receptor for HA) and NIH3T3 cells (control normal cells) [40]. To visualize the cellular uptake of the nanoreactors, we doped rhodamine B isothiocyanate (RITC) into the DMSN matrix (Fig. S23 in the ESM), obtaining fluorescently labeled nanoreactors designated as Ru-DMSNs^{RITC}@HA. Confocal microscopy images clearly showed red fluorescence in 4T1 cells after incubation with Ru-DMSNs^{RITC}@HA for 0.5 h, with fluorescence intensity increased over time (Fig. 3(a) and Fig. S24 in the ESM). In significant contrast, much weaker signals were observed in NIH3T3 cells at all time points (Fig. 3(b) and Fig. S25 in the ESM). This difference in the uptake of Ru-DMSNs^{RITC}@HA is attributed to the specific interaction between HA on the nanoreactor surface and the CD44 receptors overexpressed on 4T1 cells. Additional competition experiments further supported this conclusion, where the presence of excess free HA (5 mg/mL) blocked the uptake of Ru-DMSNs^{RITC}@HA into 4T1 cells (Fig. 3(c) and Fig. S26 in the ESM). Further, consistent with the confocal imaging data, flow cytometry analysis revealed time-dependent fluorescence enhancement in 4T1 cells (Fig. 3(d)), while no significant uptake was observed in NIH3T3 cells (Fig. 3(e)). This difference in uptake was abolished by pre-treating the cells with free HA (Figs. 3(f) and 3(g)). Therefore,

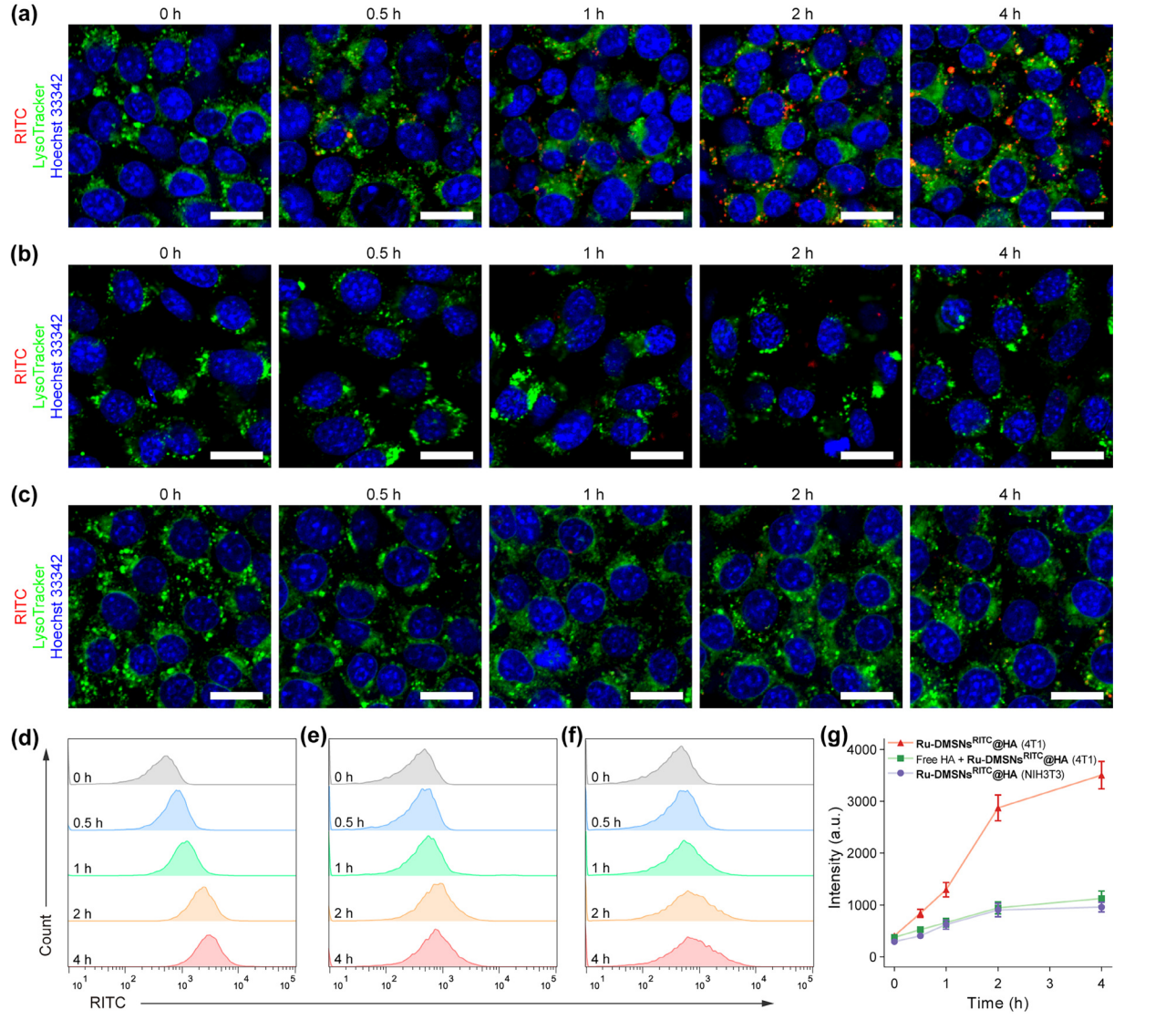

Figure 3 Cellular uptake and colocalization studies of Ru-DMSNs^{RITC}@HA. Confocal microscopy images of (a) 4T1 cells and (b) NIH3T3 cells treated with Ru-DMSNs^{RITC}@HA, and (c) 4T1 cells treated with Ru-DMSNs^{RITC}@HA in the presence of free HA (5 mg/mL) for different time. Red: RITC; green: LysoTracker; blue: Hoechst 33342. Scale bars: 20 μm. Flow cytometry analysis of (d) 4T1 cells and (e) NIH3T3 cells treated with Ru-DMSNs^{RITC}@HA, and (f) 4T1 cells treated with Ru-DMSNs^{RITC}@HA in the presence of free HA (5 mg/mL) for different time. (g) Corresponding fluorescence intensities of the histograms shown in panels (d)–(f). Data points represent mean ± s.d. (n = 3 independent experiments).

conjugation of HA bestows the nanoreactor with targeting ability, enabling selective uptake by CD44-overexpressing cancer cells.

Next, a colocalization study was conducted to track the subcellular localization of Ru-DMSNs^{RITC}@HA following receptor-mediated endocytosis in 4T1 cells. The endo-lysosomes were stained with green fluorescent LysoTracker. The intracellular fluorescence signals of Ru-DMSNs^{RITC}@HA exhibited strong colocalization with the green fluorescence of the LysoTracker (Fig. 3(a) and Fig. S24 in the ESM), suggesting that the nanoreactors were predominantly taken up through the endo-lysosomal pathway. In nature, HA turnover begins with membrane-anchored Hyal-2 degrading into large fragments of approximately fifty disaccharide units, which are then broken down by Hyal-1 into smaller pieces like tetrasaccharides after entering lysosomes [41]. Taking these natural processes into account, the cellular uptake mechanism of our nanoreactors facilitates the degradation of the surface-conjugated HA, which would allow for the opening of the gating machinery and switching on the catalytic activity of the inner immobilized Ru(II) complexes.

Subsequently, we probed the capacity of Ru-DMSNs^{RITC}@HA in mediating bioorthogonal catalysis within living cells. After incubating 4T1 cells with Ru-DMSNs^{RITC}@HA for 4 h, the culture medium was replaced with a fresh one containing alloc-RhB 110, and the intracellular fluorescence signals were analyzed by confocal microscopy and flow cytometry. Confocal microscopy revealed that, following 1 h of incubation, green fluorescence signals corresponding to liberated RhB 110 started to appear as puncta overlaying the nanoreactors. Over time, the green fluorescence gradually diffused throughout the cytosol, ultimately resulting in strong staining of the entire cytosol after 12 h (Fig. 4(a) and Fig. S27(a) in the ESM). Consistent with the confocal imaging results, flow cytometry analysis indicated that 4T1 cells treated with Ru-DMSNs^{RITC}@HA and alloc-RhB 110 showed both red and green fluorescence, with approximately 16.3-fold enhancement in the

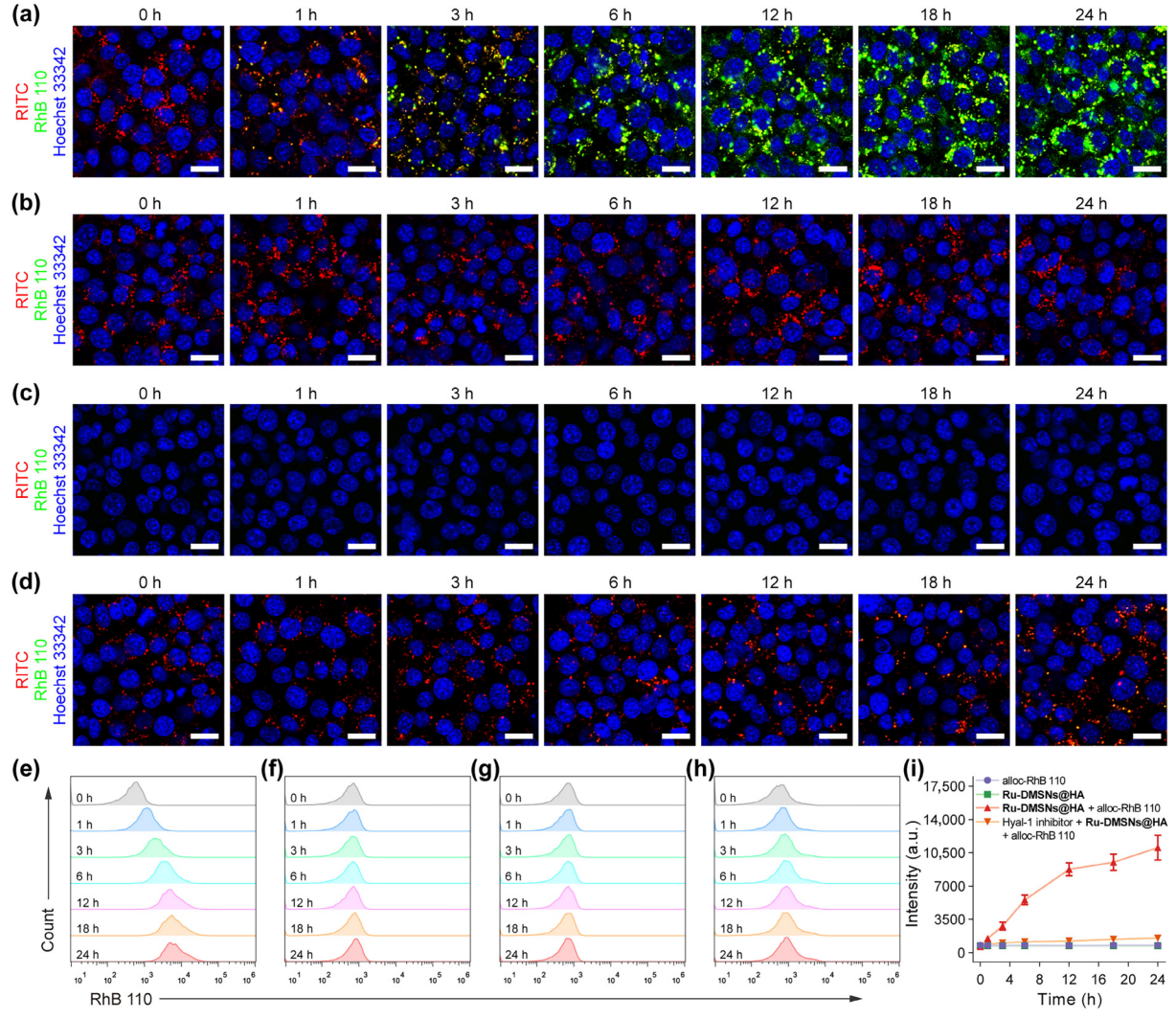

Figure 4 Ru-DMSNs^{RITC}@HA-mediated bioorthogonal catalysis in cells. Confocal microscopy images showing the fluorescence changes inside 4T1 cells after treatment with (a) Ru-DMSNs^{RITC}@HA plus alloc-RhB 110, (b) Ru-DMSNs^{RITC}@HA alone, (c) alloc-RhB 110 alone, and (d) 4T1 cells treated with Ru-DMSNs^{RITC}@HA in the presence of Hyal-1 inhibitor for different time. Red: RITC; green: RhB 110; blue: Hoechst 33342. Scale bars: 20 μm. Flow cytometry analysis of 4T1 cells treated with (e) Ru-DMSNs^{RITC}@HA plus alloc-RhB 110, (f) Ru-DMSNs^{RITC}@HA alone, (g) alloc-RhB 110 alone, and (h) 4T1 cells treated with Ru-DMSNs^{RITC}@HA in the presence of Hyal-1 inhibitor for different time. (i) Corresponding fluorescence intensities of the histograms shown in panels (e)–(h). Data points represent mean ± s.d. (n = 3 independent experiments).

green fluorescence at the end (Fig. 4(e) and Fig. S28 in the ESM). In contrast, cells treated with Ru-DMSNs^{RITC}@HA alone or alloc-RhB 110 alone did not exhibit observable green fluorescence throughout the experiments (Figs. 4(b), 4(c), 4(f) and 4(g); Figs. S27(b) and S27(c) in the ESM).

To further demonstrate the enzyme-gated behavior of Ru-DMSNs^{RITC}@HA inside cells, we performed additional experiments by co-treating 4T1 cells with neomycin sulfate (50 μg/mL), a hyaluronidase inhibitor [42]. Although the inhibitor did not affect the cellular uptake of Ru-DMSNs^{RITC}@HA, it provoked a 7.3-fold reduction in the generation of green fluorescence (Figs. 4(d), 4(h), and 4(i); Figs. S29 and S30 in the ESM). Similarly, when NIH3T3 cells, which have lower levels of CD44 receptor and Hyal-1, were treated with Ru-DMSNs^{RITC}@HA and alloc-RhB 110, very weak intracellular red and green fluorescence signals were observed (Figs. S31 and S32 in the ESM); after 24 h of incubation, only 1.3-time enhancement in green fluorescence was observed. These findings provide compelling evidence that, upon receptor-mediated endocytosis into cancer cells, the HA coating is degraded by the abundant Hyal-1, enabling the activation of the nanoreactor for catalyzing the decaging of bioorthogonal substrates. Meanwhile, the combination of the receptor-mediated specific cellular uptake mechanism and the enzymatic activation paradigm helps to minimize unintended bioorthogonal catalysis within normal cells.

3.4 In cellular synthesis of active drug

Motivated by the above encouraging results, we next investigated the ability of Ru-DMSNs@HA to selectively mediate prodrug activation within cancer cells. DOX, known for its effectiveness in treating various malignancies but accompanied by toxic side effects, was chosen as the model parent drug. To create an inactive bioorthogonal prodrug, we introduced an allyloxycarbonyl group to mask the primary amine of DOX, resulting in alloc-DOX (Scheme S5, and Figs. S33–S35 in the ESM). The efficient cleavage of the allyloxycarbonyl group on alloc-DOX by the enzyme-gated Ru-DMSNs@HA was studied in PBS and analyzed by HPLC (Figs. S36

and S37 in the ESM).

Next, a cell viability assay was performed with 4T1 and NIH3T3 cells to evaluate the antiproliferative properties of DOX, alloc-DOX, and alloc-DOX plus Ru-DMSNs@HA (50 μg/mL) at various drug concentrations (Figs. 5(a) and 5(b)). Compared to DOX, which showed a concentration-dependent and indiscriminate cytotoxicity against 4T1 (half maximal inhibitory concentration, IC_{50} = 0.71 μM) and NIH3T3 (IC_{50} = 0.29 μM) cells, alloc-DOX exhibited significantly lower efficiencies in killing both types of cells at each dose tested, underscoring that the masking group blocked the pharmaceutical activity of DOX. The IC_{50} values of alloc-DOX on 4T1 and NIH3T3 cells were determined to be 20.25 and 23.27 μM, respectively. When combined with Ru-DMSNs@HA, alloc-DOX inhibited the growth of 4T1 cells in a dose-dependent fashion with an IC_{50} value of 1.23 μM, similar to the cytotoxic profile of DOX. Conversely, when NIH3T3 cells were co-treated with Ru-DMSNs@HA and alloc-DOX, a substantially lower antiproliferative activity was observed at each prodrug dose and the corresponding IC_{50} value was approximately 12.2-time higher than that obtained with 4T1 cells. Significantly, Ru-DMSNs@HA displayed no obvious cytotoxicity towards both types of cells at concentrations up to 200 μg/mL, indicating the low cytotoxicity of the nanoreactor (Fig. S38 in the ESM).

To gain further insights into these results, we analyzed the intracellular content of DOX in these experimental groups. Consistent with the cell viability results, a similar amount of DOX was detected in 4T1 and NIH3T3 cells following incubation with the parent drug (Fig. 5(c)). However, no DOX was detected in either cell line when alloc-DOX was administered, indicating the stability of the bioorthogonally masked prodrug against nonspecific activation by biological metabolic processes. Notably, when experiments were conducted with Ru-DMSNs@HA and alloc-DOX, the amount of intracellular DOX detected in 4T1 cells was approximately 28.9-fold higher than in NIH3T3 cells (Fig. 5(c)). However, pretreatment of cells, especially 4T1 cells, with excess HA (5 mg/mL) or Hyal-1 inhibitor (50 μg/mL) greatly reduced the intracellular levels of DOX (Fig. 5c)), and correspondingly, the inhibition efficiency of cell growth was greatly reduced (Figs. 5(a) and 5(b)). These results highlight that our enzyme-gated bioorthogonal catalytic nanoreactor, equipped with cancer targeting capacity and intracellular enzyme-responsive machinery, can specifically mediate prodrug activation within cancer cells while sparing normal cells.

Furthermore, we delineated the mechanism of cell death in 4T1 cells treated with Ru-DMSNs@HA plus alloc-DOX by double-staining flow cytometric and TUNEL assays. Like the results

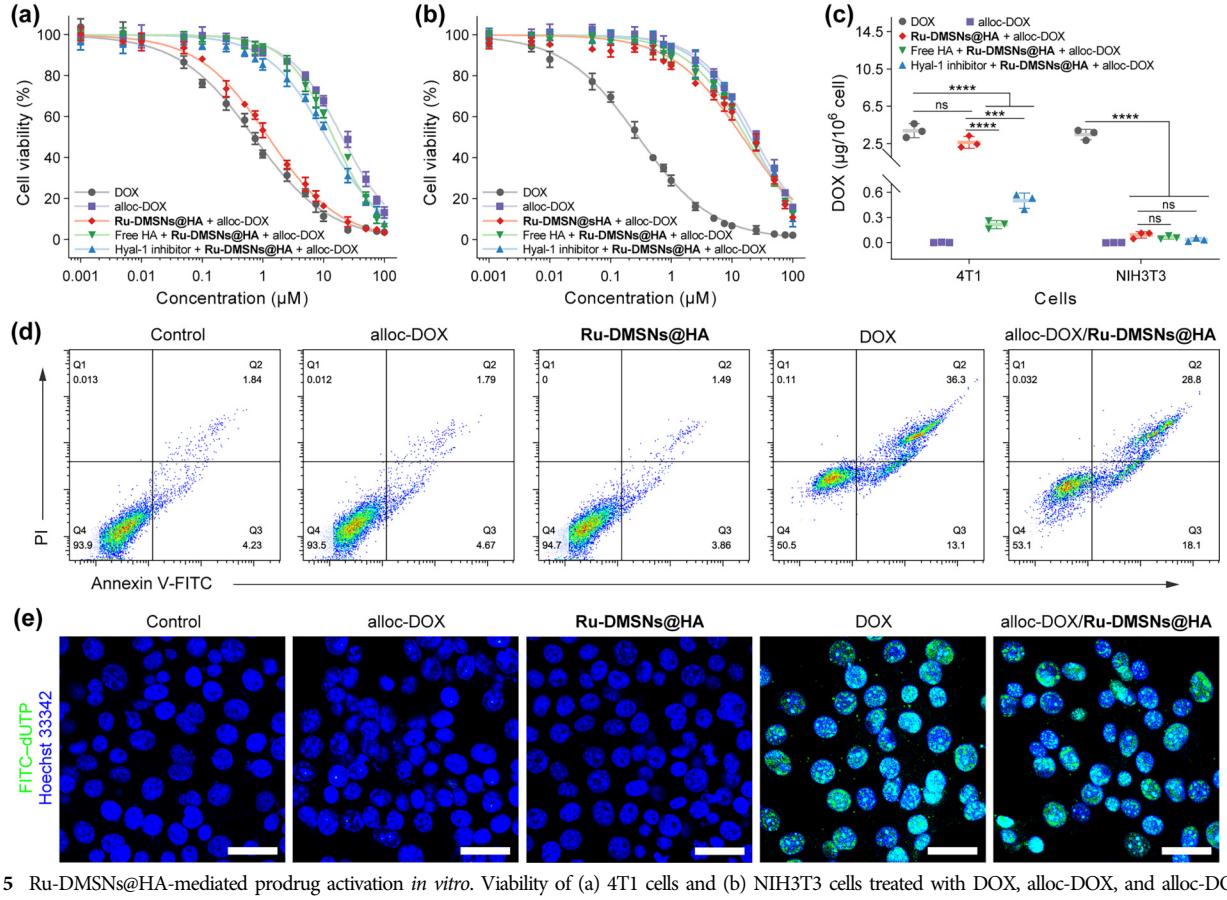

Figure 5 Ru-DMSNs@HA-mediated prodrug activation *in vitro*. Viability of (a) 4T1 cells and (b) NIH3T3 cells treated with DOX, alloc-DOX, and alloc-DOX/Ru-DMSNs@HA combination in the absence and presence of free HA (5 mg/mL, 2 h) or Hyal-1 inhibitor (50 μg/mL, 6 h) plus alloc-DOX/Ru-DMSNs@HA combination at different drug concentrations. (c) Intracellular DOX levels in 4T1 and NIH3T3 cells after 24 h of treatment with the alloc-DOX/Ru-DMSNs@HA combination, with or without pretreatment of HA (5 mg/mL, 2 h) or Hyal-1 inhibitor (50 μg/mL, 6 h). (d) Flow cytometry analysis of the 4T1 cell apoptosis at 24 h after treatment with 1% DMSO, alloc-DOX, Ru-DMSNs@HA, DOX, and Ru-DMSNs@HA plus alloc-DOX. (e) Confocal microscopy images of 4T1 cells stained with FITC-dUTP (green, TUNEL assay) and Hoechst 33342 (blue, nuclei staining) after different treatments. In (d) and (e), the control group was treated with vehicle. Scale bars: 50 μm. (a)–(c) data points were presented as mean ± s.d. (n = 3 independent experiments). Statistical significance was calculated via one-way ANOVA analysis with a Tukey post-hoc test or two-tailed Student's t-test (***P < 0.001, ****P < 0.0001. ns, not significant).

obtained with DOX, co-treatment of Ru-DMSNs@HA and alloc-DOX elicited a high percentage (46.9%) of Annexin-V positive cells (Fig. 5(d)) and strong fluorescent signals in TUNEL staining (Fig. 5(e)), implying that 4T1 cells underwent apoptosis. However, no evident apoptotic cell death was seen in control groups treated with vehicle, alloc-DOX, or Ru-DMSNs@HA. Taken together, these findings demonstrate that the specific cytotoxicity observed in 4T1 cells receiving Ru-DMSNs@HA and alloc-DOX combinational treatment originated from the intracellular conversion of alloc-DOX into DOX through enzyme-gated bioorthogonal catalysis.

3.5 Bioorthogonal prodrug activation *in vivo* for cancer therapy

Prior to assessing the potency of Ru-DMSNs@HA in activating alloc-DOX within tumors, we conducted pharmacokinetics and biodistribution studies following intravenous injection of the nanoreactor (20 mg/kg) into 4T1 tumor-bearing mice. To highlight the significance of covalently immobilizing TMCs within HA-conjugated DMSNs, we included additional experiments conducted with "naked" fRu as a control. We found that, compared to fRu, which exhibited a short blood circulation half-life ($t_{1/2}$) of 0.48 h, Ru-DMSNs@HA exhibited a prolonged $t_{1/2}$ of 3.7 h (Fig. S39(a) in the ESM). The concentration-time profiles and corresponding area under the curves (AUCs) indicated that Ru-DMSNs@HA achieved significantly higher exposure of Ru within tumors compared to fRu (Fig. S39(b) in the ESM). Additionally, while fRu was primarily cleared by the renal system (Fig. 6(a)), Ru-DMSNs@HA showed significant accumulation in clearance organs such as the liver and spleen (Fig. 6(b)), typical for nanoparticle biodistribution in mice [43]. In parallel, we studied the stability of catalysts *in vivo*, focusing

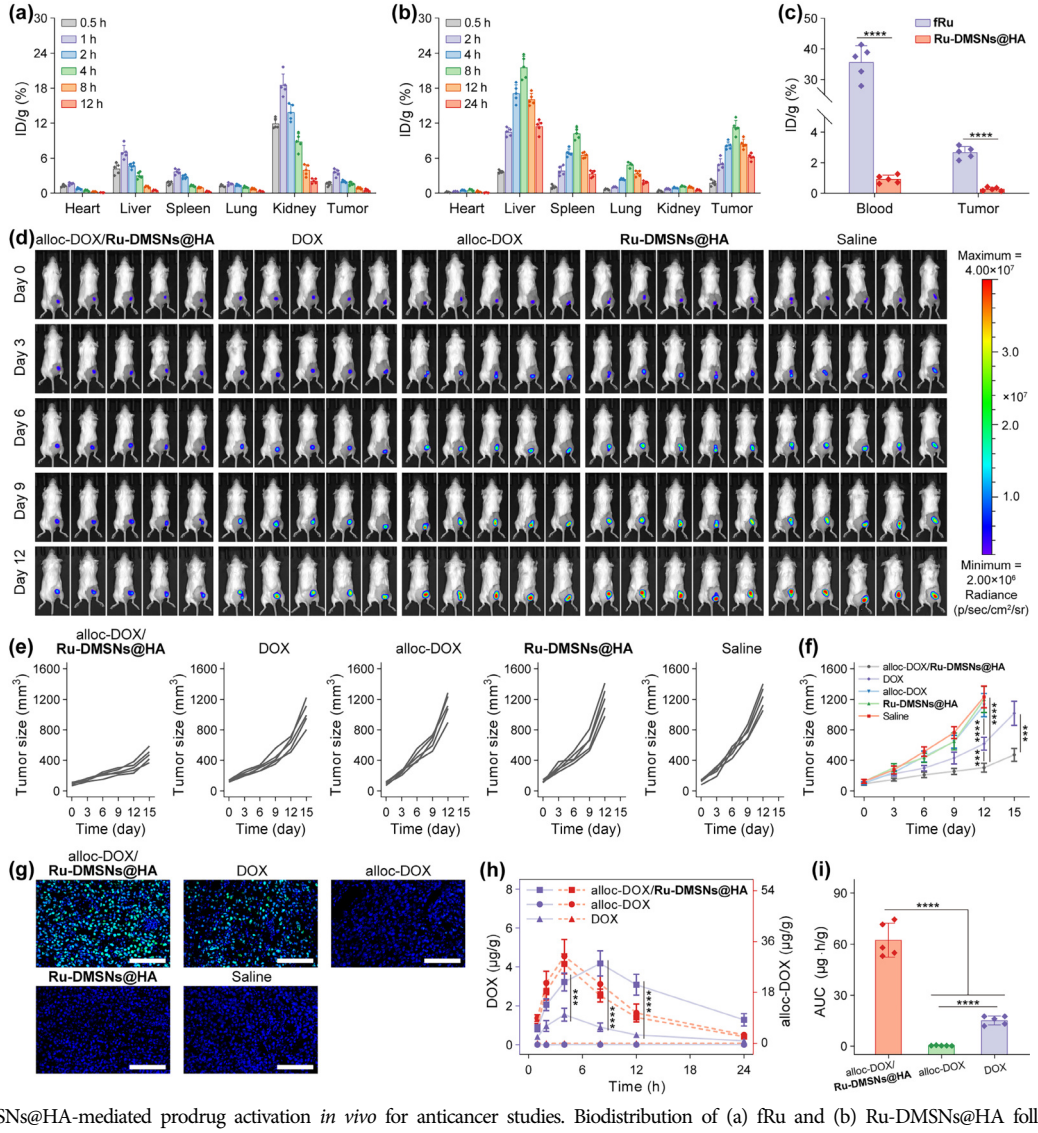

Figure 6 Ru-DMSNs@HA-mediated prodrug activation *in vivo* for anticancer studies. Biodistribution of (a) fRu and (b) Ru-DMSNs@HA following intravenous injection over different time points. (c) Quantification of Ru leakage from Ru-DMSNs@HA in blood circulation and Ru washout from tumor tissues. Experiments conducted with fRu were set as the control. (d) Bioluminescence imaging of the 4T1 tumor growth in mice treated with the alloc-DOX/Ru-DMSNs@HA combination, DOX, alloc-DOX, Ru-DMSNs@HA or saline. (e) Individual tumor growth kinetics of mice for each treatment group. (f) Changes in average tumor sizes across the treatment groups. (g) Analysis of cell death mechanism in the tumor tissues after different treatments, with FITC-dUTP (green, TUNEL assay) for apoptosis and Hoechst 33342 (blue) for nuclei staining. Scale bars: 100 μm. (h) Drug and prodrug concentrations versus time in tumors after different treatments. (i) The corresponding AUCs of the exposure of DOX to tumors in alloc-DOX/Ru-DMSNs@HA combination, alloc-DOX and DOX groups. Data points were presented as mean ± s.d. (n = 5 mice). Statistical significance was calculated via one-way ANOVA analysis with a Tukey post-hoc test or two-tailed Student's t-test (***P < 0.001, ****P < 0.0001).

on their potential leaching from the nanoscaffold during blood circulation and washout from tumor cells. At time points corresponding to their respective peak concentrations, blood samples were collected, and tumors were exercised and digested to obtain tumor cells. These samples were then mixed with PBS, gently shaken for 24 h, and subjected to ultracentrifugation. Analysis of the Ru content in the resulting filter revealed no unexpected metal leakage occurred in the blood samples collected from Ru-DMSNs@HA group. Moreover, there was unobvious washout of Ru from tumor cells in the group treated with Ru-DMSNs@HA compared to the fRu group (Fig. 6(c)). These results suggest that the prolonged circulation of nanoreactor, combined with the EPR effect, the gatekeeper and targeting ability of HA, and the covalent immobilization of organometals within nanoscafflods collectively promote the accumulation and retention of TMCs within tumors while minimizing unexpected catalyst leaching.

We then evaluated the ability of Ru-DMSNs@HA in activating alloc-DOX for cancer therapy using xenograft 4T1 tumor-bearing mice. Mice were randomly divided into five groups and treated with saline, DOX (5 mg/kg), alloc-DOX (100 mg/kg), Ru-DMSNs@HA (20 mg/kg), and Ru-DMSNs@HA (20 mg/kg) plus alloc-DOX (100 mg/kg). The treatments were administered once every three days over a two-week period. DOX and alloc-DOX were administered via intraperitoneal injection, while Ru-DMSNs@HA was administered intravenously. In the combinational treatment group, alloc-DOX was given 6 h following the administration of Ru-DMSNs@HA. The therapeutic outcomes were assessed by measuring bioluminescence signals and recording tumor volumes. As shown in Figs. 6(d)–6(f), like the saline group, neither alloc-DOX nor Ru-DMSNs@HA alone prevented tumor growth, indicating a lack of antitumor effect from the prodrug or the nanoreactor. Compared to DOX, which demonstrated a moderate therapeutic effect, the combined Ru-DMSNs@HA and alloc-DOX treatment was significantly more effective at slowing tumor growth. Furthermore, TUNEL staining of tumor sections revealed strong apoptotic signals in groups treated with DOX and the combination of Ru-DMSNs@HA and alloc-DOX but not in other groups (Fig. 6(g)), which suggested a similarity in the pharmacological mechanism between DOX and Ru-DMSNs@HA/alloc-DOX combinational treatment.

To better understand the therapeutic outcomes, we analyzed DOX levels in the plasma, major organs, and tumors versus time. As shown in Fig. 6(h) and Fig. S40 in the ESM, no DOX was detected in all tissues of the alloc-DOX-treated mice, indicating the bioorthogonality of alloc-DOX against nonspecific biological cleavage in complex living systems. The concentration of DOX detected in the combinational treatment group was significantly higher at 4, 8 and 12 h post administration compared to the DOX group. Analysis of the AUCs revealed that the exposure of DOX to tumors in the combinational treatment group was approximately 4.1 times higher than that yielded by DOX (Fig. 6(i)). Despite alloc-DOX being administered at a 20-fold higher dose than DOX, the plasma and major organs of mice receiving dual Ru-DMSNs@HA and alloc-DOX treatment exhibited significantly lower exposure to DOX compared to the DOX-treated group (Fig. S40 in the ESM). Although there was a time overlap between Ru and alloc-DOX in the clearance organs like liver, spleen, and kidney in the combinational treatment group, the limited off-target prodrug activation might be due to the distinct clearance mechanisms between nanoparticles and small-molecule agents [43–45] (such as their uptake in different cell populations or subcellular distribution), the avoided catalyst leaching, and the gated mechanism of the nanoreactor. These factors together minimized the chances for alloc-DOX and Ru(II) complexes to meet at nontargeted sites. Overall, these findings provide comprehensive evidence that the cancer-specific intracellular activation mechanism of the enzyme-gated bioorthogonal nanoreactor enables the decaging of alloc-DOX primarily within tumors while minimizing drug exposure to nontargeted organs and tissues.

Lastly, we assessed the biosafety of our bioorthogonal prodrug activation strategy. Like the control group, no dramatic fluctuations in the bodyweight were observed for mice receiving different treatments (Fig. S41 in the ESM). H&E staining of the major organs revealed no observable signs of pathological damage or inflammation across all groups (Fig. S42 in the ESM). Also, the serum levels of typical inflammatory cytokines, such as tumor necrosis factor-α, interleukin-6/12, and interferon-γ, in the treated mice showed no statistical differences compared to control group (Fig. S43 in the ESM). In addition, blood chemistry analysis revealed no signs of hepatic or renal toxicity induced by the nanoreactor or prodrug (Figs. S44 and S45 in the ESM). Thus, these results demonstrate that Ru-DMSNs@HA and alloc-DOX (even given at a high dose) were well tolerated and, particularly, the nanoreactor can mediate bioorthogonal prodrug activation for cancer therapy in a safe way.

4 Conclusions

In summary, we have successfully developed a tumor microenvironment-responsive bioorthogonal catalytic nanoreactor using HA-coated DMSNs as a nanoscaffold for the covalent immobilization of organometal catalysts. Our study demonstrated the high effectiveness of this nanoreactor in converting inactive prodrugs into active drugs in both *in vitro* and *in vivo* models. The covalent binding of Ru(II) catalyst to DMSNs and capping the surface with HA prevent unexpected metal leakage and off-target catalyst deposition, which not only broadens the therapeutic window but also minimizes drug exposure in normal organs and tissues. Furthermore, the surface coating of DMSNs with HA ensures high stability, excellent biocompatibility, and effective accumulation within tumors. Importantly, our results evidenced that these nanoreactors specifically targeted tumor sites, where catalyst activity was restored for *in situ* prodrug activation, effectively inhibiting tumor growth and mitigating side effects. Overall, this work would inspire the development of advanced bioorthogonal catalytic devices with gated controllability for *in situ* prodrug conversion in complex organisms, enabling the manipulation of diseases beyond cancer in a safe and effect way.

Electronic Supplementary Material: Supplementary material (further details of the synthesis of CpRu(η^3-allyl)(QL-Mal)]PF_6 and fRu, XPS spectrum, confocal microscopy images, flow cytometry cytograms, blood circulation curve, drug and prodrug concentrations versus time in tissues, hematoxylin and eosin-stained images, blood biochemical and hematological analysis, the ^{1}H NMR, ^{13}C NMR and HRMS spectra of all compounds) is available in the online version of this article at https://doi.org/10.26599/NR.2025.94907134.

Data availability

All data needed to support the conclusions in the paper are presented in the manuscript and the Electronic Supplementary

Material. Additional data related to this paper may be requested from the corresponding author upon request.

Acknowledgments

This work was funded by the National Key Research and Development Program of China (No. 2020YFA0210800, H. H. Y.), the Major Project of Science and Technology of Fujian Province (No. 2020HZ06006, H. H. Y.), the National Natural Science Foundation of China (Nos. 22421002, 22027805, and 22334004, H. H. Y.; Nos. 22107019, and 22277011, Z. W. C.; No. 22404025, Y. H. Y.), and the Research project of General Administration of Customs of PRC (No. 2024HK008, X. H. Z.).

Declaration of competing interest

All the other contributing authors report no conflict of interests in this work. Author Zhaowei Chen is the Young Star Editor of this journal, but he is not involved in the peer-review or decision of this article.

Author contribution statement

Y. H., Y. H. Y., and Z. W. C. directed the research. Y. H. G., Y. H. Y., and Z. W. C. conceptualized and designed the experiments. Y. H. G., F. J., X. H. Z., W. H., S. J. S., X. C. S., M. N. W., T. W., T. J. H., Z. Y., and X. Y. W. collected and analyzed the data. Z. W. C. wrote manuscript. Z. T. C., Y. H., Y. H. Y., Z. W. C., and H. H. Y. polished and revised the manuscript. X. H. Z., Y. H. Y., Z. W. C., and H. H. Y. acquired the fundings.

Informed consent

Not applicable.

Ethics statement

The animal experiments were carried out following the guidelines of the Institutional Animal Care and Use Committee of Fuzhou University (Ethical code: 013-20200610-002).

Use of AI statement

None.

References

[1] Scinto, S. L.; Bilodeau, D. A.; Hincapie, R.; Lee, W.; Nguyen, S. S.; Xu, M. H.; am Ende, C. W.; Finn, M. G.; Lang, K.; Lin, Q. et al. Bioorthogonal chemistry. *Nat. Rev. Methods Primers* **2021**, *1*, 30.

[2] Pani, S.; Qiu, T.; Kentala, K.; Azizi, S. A.; Dickinson, B. C. Bioorthogonal masked acylating agents for proximity-dependent RNA labelling. *Nat. Chem.* **2024**, *16*, 717–726.

[3] Zhu, Y. C.; Ding, W. L.; Chen, Y. L.; Shan, Y.; Liu, C.; Fan, X. Y.; Lin, S. X.; Chen, P. R. Genetically encoded bioorthogonal tryptophan decaging in living cells. *Nat. Chem.* **2024**, *16*, 533–542.

[4] Li, J.; Chen, P. R. Development and application of bond cleavage reactions in bioorthogonal chemistry. *Nat. Chem. Biol.* **2016**, *12*, 129–137.

[5] Wang, X. Z.; Liew, S. S.; Huang, J. S.; Hu, Y. X.; Wei, X.; Pu, K. Y. Dual-locked enzyme-activatable bioorthogonal fluorescence turn-on imaging of senescent cancer cells. *J. Am. Chem. Soc.* **2024**, *146*, 22689–22698.

[6] Liao, X. F.; Qin, G.; Liu, Z. Q.; Ren, J. S.; Qu, X. G. Bioorthogonal aptamer-ATTEC conjugates for degradation of alpha-synuclein via autophagy-lysosomal pathway. *Small* **2024**, *20*, 2306760.

[7] Song, J. L.; Wu, C. L.; Zhao, Y.; Yang, M.; Yao, Q. X.; Gao, Y. Bioorthogonal disassembly of tetrazine bearing supramolecular assemblies inside living cells. *Small* **2022**, *18*, 2104772.

[8] Liu, Z. W.; Sun, M. Y.; Zhang, W. T.; Ren, J. S.; Qu, X. G. Target-specific bioorthogonal reactions for precise biomedical applications. *Angew. Chem., Int. Ed.* **2023**, *62*, e202308396.

[9] Liu, X.; Huang, T. J.; Chen, Z. W.; Yang, H. H. Progress in controllable bioorthogonal catalysis for prodrug activation. *Chem. Commun.* **2023**, *59*, 12548–12559.

[10] Liang, T. X. Z.; Chen, Z. W.; Li, H. J.; Gu, Z. Bioorthogonal catalysis for biomedical applications. *Trends Chem.* **2022**, *4*, 157–168.

[11] Huang, R.; Hirschbiegel, C. M.; Lehot, V.; Liu, L.; Cicek, Y. A.; Rotello, V. M. Modular fabrication of bioorthogonal nanozymes for biomedical applications. *Adv. Mater.* **2024**, *36*, 2300943.

[12] Bai, Y. G.; Chen, J. F.; Zimmerman, S. C. Designed transition metal catalysts for intracellular organic synthesis. *Chem. Soc. Rev.* **2018**, *47*, 1811–1821.

[13] James, C. C.; de Bruin, B.; Reek, J. N. H. Transition metal catalysis in living cells: Progress, challenges, and novel supramolecular solutions. *Angew. Chem., Int. Ed.* **2023**, *62*, e202306645.

[14] Chen, Z. W.; Li, H. J.; Bian, Y. J.; Wang, Z. J.; Chen, G. J.; Zhang, X. D.; Miao, Y. M.; Wen, D.; Wang, J. Q.; Wan, G. et al. Bioorthogonal catalytic patch. *Nat. Nanotechnol.* **2021**, *16*, 933–941.

[15] Weiss, J. T.; Dawson, J. C.; Macleod, K. G.; Rybski, W.; Fraser, C.; Torres-Sánchez, C.; Patton, E. E.; Bradley, M.; Carragher, N. O.; Unciti-Broceta, A. Extracellular palladium-catalysed dealkylation of 5-fluoro-1-propargyl-uracil as a bioorthogonally activated prodrug approach. *Nat. Commun.* **2014**, *5*, 3277.

[16] Bray, T. L.; Salji, M.; Brombin, A.; Pérez-López, A. M.; Rubio-Ruiz, B.; Galbraith, L. C. A.; Patton, E. E.; Leung, H. Y.; Unciti-Broceta, A. Bright insights into palladium-triggered local chemotherapy. *Chem. Sci.* **2018**, *9*, 7354–7361.

[17] Ji, X. Y.; Pan, Z. X.; Yu, B. C.; De La Cruz, L. K.; Zheng, Y. Q.; Ke, B. W.; Wang, B. H. Click and release: Bioorthogonal approaches to "on-demand" activation of prodrugs. *Chem. Soc. Rev.* **2019**, *48*, 1077–1094.

[18] Sousa-Castillo, A.; Mariño-López, A.; Puértolas, B.; Correa-Duarte, M. A. Nanostructured heterogeneous catalysts for bioorthogonal reactions. *Angew. Chem., Int. Ed.* **2023**, *62*, e202215427.

[19] Hirschbiegel, C. M.; Zhang, X. Z.; Huang, R.; Cicek, Y. A.; Fedeli, S.; Rotello, V. M. Inorganic nanoparticles as scaffolds for bioorthogonal catalysts. *Adv. Drug Deliv. Rev.* **2023**, *195*, 114730.

[20] Chen, Y. Y.; Wu, T.; Xie, S. S.; Bai, Y. G.; Xing, H. Orientation-controlled membrane anchoring of bioorthogonal catalysts on live cells via liposome fusion-based transport. *Sci. Adv.* **2023**, *9*, eadg2583.

[21] Rubio-Ruiz, B.; Pérez-López, A. M.; Uson, L.; Ortega-Liebana, M. C.; Valero, T.; Arruebo, M.; Hueso, J. L.; Sebastian, V.; Santamaria, J.; Unciti-Broceta, A. *In cellulo* bioorthogonal catalysis by encapsulated AuPd nanoalloys: Overcoming intracellular deactivation. *Nano Lett.* **2023**, *23*, 804–811.

[22] Tonga, G. Y.; Jeong, Y.; Duncan, B.; Mizuhara, T.; Mout, R.; Das, R.; Kim, S. T.; Yeh, Y. C.; Yan, B.; Hou, S. et al. Supramolecular regulation of bioorthogonal catalysis in cells using nanoparticle-embedded transition metal catalysts. *Nat. Chem.* **2015**, *7*, 597–603.

[23] Sancho-Albero, M.; Rubio-Ruiz, B.; Pérez-López, A. M.; Sebastián, V.; Martín-Duque, P.; Arruebo, M.; Santamaría, J.; Unciti-Broceta, A. Cancer-derived exosomes loaded with ultrathin palladium nanosheets for targeted bioorthogonal catalysis. *Nat. Catal.* **2019**, *2*, 864–872.

[24] Yusop, R. M.; Unciti-Broceta, A.; Johansson, E. M. V.; Sánchez-Martín, R. M.; Bradley, M. Palladium-mediated intracellular chemistry. *Nat. Chem.* **2011**, *3*, 239–243.

[25] Zeng, F.; Pan, Y. C.; Wu, M. N.; Lu, Q. L.; Qin, S. R.; Gao, Y. F.;

Luan, X. W.; Chen, R. Y.; He, G. Z.; Wang, Y. Z. et al. Self-metallized whole cell vaccines prepared by microfluidics for bioorthogonally catalyzed antitumor immunotherapy. *ACS Nano* **2024**, *18*, 7923–7936.

[26] Cao, S. P.; Ivanov, T.; Heuer, J.; Ferguson, C. T. J.; Landfester, K.; Caire da Silva, L. Dipeptide coacervates as artificial membraneless organelles for bioorthogonal catalysis. *Nat. Commun.* **2024**, *15*, 39.

[27] Zhang, X. Z.; Lin, S. C.; Huang, R.; Gupta, A.; Fedeli, S.; Cao-Milán, R.; Luther, D. C.; Liu, Y. C.; Jiang, M. D.; Li, G. et al. Degradable ZnS-supported bioorthogonal nanozymes with enhanced catalytic activity for intracellular activation of therapeutics. *J. Am. Chem. Soc.* **2022**, *144*, 12893–12900.

[28] Zhang, L.; Sang, Y. J.; Liu, Z. Q.; Wang, W. J.; Liu, Z. W.; Deng, Q. Q.; You, Y. W.; Ren, J. S.; Qu, X. G. Liquid metal as bioinspired and unusual modulator in bioorthogonal catalysis for tumor inhibition therapy. *Angew. Chem., Int. Ed.* **2023**, *62*, e202218159.

[29] Kumar, A.; Lee, I. S. Designer nanoreactors for bioorthogonal catalysis. *Acc. Chem. Res.* **2024**, *57*, 413–427.

[30] Burdick, J. A.; Prestwich, G. D. Hyaluronic acid hydrogels for biomedical applications. *Adv. Mater.* **2011**, *23*, H41–H56.

[31] He, Y. M.; Lei, L.; Cao, J.; Yang, X. T.; Cai, S. S.; Tong, F.; Huang, D.; Mei, H.; Luo, K.; Gao, H. L. et al. A combinational chemo-immune therapy using an enzyme-sensitive nanoplatform for dual-drug delivery to specific sites by cascade targeting. *Sci. Adv.* **2021**, *7*, eaba0776.

[32] Toole, B. P. Hyaluronan: From extracellular glue to pericellular cue. *Nat. Rev. Cancer* **2004**, *4*, 528–539.

[33] Chen, Z. W.; Zhao, C. Q.; Ju, E. G.; Ji, H. W.; Ren, J. S.; Binks, B. P.; Qu, X. G. Design of surface-active artificial enzyme particles to stabilize pickering emulsions for high-performance biphasic biocatalysis. *Adv. Mater.* **2016**, *28*, 1682–1688.

[34] Hunter, R. J. *Zeta Potential in Colloid Science: Principles and Applications*; Academic Press: London, 1981.

[35] Dai, J. D.; Liu, Z.; Wang, L. L.; Huang, G. M.; Song, S. J.; Chen, C.; Wu, T.; Xu, X.; Hao, C. J.; Bian, Y. J. et al. A telomerase-activated magnetic resonance imaging probe for consecutively monitoring tumor growth kinetics and *in situ* screening inhibitors. *J. Am. Chem. Soc.* **2023**, *145*, 1108–1117.

[36] van der Meel, R.; Sulheim, E.; Shi, Y.; Kiessling, F.; Mulder, W. J. M.; Lammers, T. Smart cancer nanomedicine. *Nat. Nanotechnol.* **2019**, *14*, 1007–1017.

[37] Copéret, C.; Allouche, F.; Chan, K. W.; Conley, M. P.; Delley, M. F.; Fedorov, A.; Moroz, I. B.; Mougel, V.; Pucino, M.; Searles, K. et al. Bridging the gap between industrial and well-defined supported catalysts. *Angew. Chem., Int. Ed.* **2018**, *57*, 6398–6440.

[38] Mo, R.; Jiang, T. Y.; DiSanto, R.; Tai, W. Y.; Gu, Z. ATP-triggered anticancer drug delivery. *Nat. Commun.* **2014**, *5*, 3364.

[39] Liu, G.; Choi, K. Y.; Bhirde, A.; Swierczewska, M.; Yin, J.; Lee, S. W.; Park, J. H.; Hong, J. I.; Xie, J.; Niu, G. et al. Sticky nanoparticles: A platform for siRNA delivery by a Bis(zinc(II) dipicolylamine)-functionalized, self-assembled nanoconjugate. *Angew. Chem., Int. Ed.* **2012**, *51*, 445–449.

[40] Lv, Y. Q.; Xu, C. R.; Zhao, X. M.; Lin, C. S.; Yang, X.; Xin, X. F.; Zhang, L.; Qin, C.; Han, X. P.; Yang, L. et al. Nanoplatform assembled from a CD44-targeted prodrug and smart liposomes for dual targeting of tumor microenvironment and cancer cells. *ACS Nano* **2018**, *12*, 1519–1536.

[41] Stern, R. Hyaluronan catabolism: A new metabolic pathway. *Eur. J. Cell Biol.* **2004**, *83*, 317–325.

[42] Duan, H. H.; Donovan, M.; Hernandez, F.; Di Primo, C.; Garanger, E.; Schultze, X.; Lecommandoux, S. Hyaluronic-acid-presenting self-assembled nanoparticles transform a hyaluronidase HYAL1 substrate into an efficient and selective inhibitor. *Angew. Chem., Int. Ed.* **2020**, *59*, 13591–13596.

[43] Wilhelm, S.; Tavares, A. J.; Dai, Q.; Ohta, S.; Audet, J.; Dvorak, H. F.; Chan, W. C. W. Analysis of nanoparticle delivery to tumours. *Nat. Rev. Mater.* **2016**, *1*, 16014.

[44] Cabral, H.; Li, J. J.; Miyata, K.; Kataoka, K. Controlling the biodistribution and clearance of nanomedicines. *Nat. Rev. Bioeng.* **2024**, *2*, 214–232.

[45] Miller, M. A.; Mikula, H.; Luthria, G.; Li, R.; Kronister, S.; Prytyskach, M.; Kohler, R. H.; Mitchison, T.; Weissleder, R. Modular nanoparticulate prodrug design enables efficient treatment of solid tumors using bioorthogonal activation. *ACS Nano* **2018**, *12*, 12814–12826.